UNIVERSITAT POLITÈCNICA DE VALÈNCIA

CMT - Heat Engines University Institute

Development of CFD model for the study of the potential of oxymethylene ethers for soot reduction in medium duty compression ignition engines

Master's Thesis

Master's Degree in Reciprocating Internal Combustion Engines

AUTHOR: Khalid , Usama Bin

Tutor: Micó Reche, Carlos

ACADEMIC YEAR: 2021/2022

TRABAJO DE FIN DE MÁSTER

Development of CFD model for the study of the potential of oxymethylene ethers for soot reduction in medium duty compression ignition engines

Realizado por: Usama Bin Khalid
Dirigido por: Carlos Micó Reche

Valencia, septiembre de 2022

Máster Universitario en
Motores de Combustión Interna Alternativos,
curso 2021-2022

INSTITUTO UNIVERSITARIO CMT-MOTORES TÉRMICOS

Abstract

The reduction of the carbon footprint of internal combustion engines and the pollutant emissions is mandatory for the survival of this technology especially for medium and heavy duty. In this sense, e-fuels (also termed as synthetic fuels) are considered as a potential pathway to achieve this reduction and even a remarkable carbon footprint mitigation in compression ignition (CI) engines. Among numerous e-fuels, oxymethylene ethers (OME_x) stand out because of their low soot formation characteristics. However, the complexity of their physical and chemical properties makes it a challenge to be used in conventional engines.

The aim of this work is to develop a Computational Fluid Dynamic (CFD) model to investigate the effect of the stoichiometry of OME_x on the in-cylinder combustion behavior and the pollutant formation when blended with fossil Diesel. The model is based on a medium duty CI engine and has been developed with the software CONVERGE CFD. Experimental data, gathered from optical engine based on the same geometry, is used to adjust the different sub-models, and validate numerical simulation results. In a first approach, different reaction mechanism that can be found in the literature were evaluated to identify the most appropriate one, using n-heptane as the fossil diesel surrogate and OME_3 as the OME_x surrogate. In a second approach, a reduced reaction mechanism is developed to simulate the combustion of OME_x – fossil diesel blends with more complex surrogate fuels, that could reproduce with more accuracy the behavior of the originals.

The numerical simulations highlight the differences in terms of equivalence ratio fields achieved when varying the e-fuel content in the blend. Therefore, the combustion process is faster, and the soot formation is drastically reduced when the oxymethylene ethers content is above 30%. This makes these blends interesting to reduce the well-known soot-NO_x trade off of compression ignition engines.

Contents

1 Introduction

The contribution of the transport sector to the greenhouse effect and global warming is well known. It has been reported that the transportation sector is responsible for almost 18% of total CO_2 emitted in energy sector in european union (EU) [1] while heavy duty vehicles contribute with more than 25% of the total EU green house gas (GHG) emissions from road transport sector [2]. On top of that, diesel operated vehicles have additional significant emissions-related problems, due to their well known soot-NO_x trade off [3]. Besides, studies reveal that the direct vehicle emissions related to particulate matter are predominantly generated by diesel vehicles [4]. For this reason, increasingly restrictive regulation are put in place to limit the environmental impact. To face this situation, a great amount of research is being carried out and different pathways have been defined. In the last years, the implementation of hybridization and electrification in power trains [5] has gained lot of attention. Even most of the main automotive manufactures have chosen this approach to achieve the desired emission reduction. However, for certain applications (heavy duty) or in certain markets the electrification is not clear in short or medium term. In these scenarios, the internal combustion engines will still play a major role and the use of renewable fuels to replace the conventional ones will allow to achieve a reduction of fossil fuel dependency and cleaner combustion [6]. These fuels are manufactured by using renewable energy. In fact, they are considered as ways of renewable energy storage and transportation. They can be bio-fuels [7] if they are produced from biomass or synthetic fuels, also known as e-fuels [8]. Focusing on the last ones, they are considered a promising alternative to drastically reduce engines carbon footprint and even achieve carbon neutrality [6]. Primarily these fuels are produced from electrolysis of water, converting this molecule into their individual components (H_2 and O_2) [9], and from carbon capture for obtaining CO_2 [10] that is later used as the carbon source for e-fuels production. The use of CO_2 for its production as well as renewable energy sources contribute to reduce its carbon footprint and to achieve carbon neutrality [8].

Among the e-fuels category, oxygenated dimethyl ether (OME_x) also termed as polyoxymethylene dimethyl ether (PODE) have been widely considered as an interesting alternative to fossil diesel due to their very low soot formation during the combustion process [11]. OME_x have a molecular structure of CH_3-O-$(CH_2$-O$)_x$-CH_3 where x ranges from 1 to 6. This fuel has high oxygen content in their molecular composition without any C-C bond, which are the main reasons for low soot formation during combustion [12]. Furthermore, OME_x have a high cetane number (CN), which mainly depends upon the degree of polymerization, that is usually higher than that of fossil diesel. In fact the CN of OME_x exceeds 60 when x is larger than 1 [13]. Moreover the resemblance of the physical properties of OME_x with those of fossil diesel makes it a perfect fuel to be used as a blend with fossil diesel in any ratio [6][14]. So, thanks to these characteristics, OME_x has been of great interest for researchers for the past few years. Numerous detailed experimental studies have reported a significant reduction in soot and PM emissions either using neat OME_x or OME_x blend with fossil diesel [15][16][17]. It has also been reported that this fuel allows to use high rates of exhaust gas recirculation (EGR) to reduce NO_x without penalizing the soot formation, which ultimately leads to the reduction of the soot-NO_x trade off [18]. The life cycle analysis of OME_x presented by Benajes et al. [19] resulted in reduction of well-to-wheel carbon emissions of up to 19% as compared to diesel-gasoline dual fuel mode, mainly due to OME_x production process which requires carbon capture and a clean electric energy source. In addition, Hank et al. [20] presented OME_x as a potential solution to bring down local PM and NO_x emissions.

Nowadays multi-dimensional computational fluid dynamics (CFD) simulations coupled with chemical kinetics have also emerged as a comprehensive tool to be used to deeply understand

combustion process [21]. To the authors knowledge, few numerical studies about blends of fossil diesel with OME_x have been carried out in recent years. These studies are mainly focused on the development of the reaction mechanism needed for their simulation, in turn validating their numerical model with an experimental dataset. In 2016, Sun et al [22] developed a high temperature kinetic mechanism for OME_3 and validated it against experimental results. His study highlighted that, owing to the absence of C-C bonds in the C-O chain structure, a significant reduction of soot was achieved. Later He at al. [23] constructed a detailed mechanism for OME_x combustion for low and medium temperature engine applications. Their results were widely validated against ignition delay data and combustion under HCCI conditions. Following his work, Ren et al. [24] created a reduced OME_x-diesel mechanism. Their work was also validated in terms of ignition delay, flame speed and combustion under HCCI conditions. Further, numerical simulations of a direct injection compression ignition (DICI) engine were also performed ,which confirmed that the use of high OME_x content in the blends greatly reduced soot emissions. Lv et al. [25] reported that the more we add OME_x in the blend, the more the air-fuel mixing was promoted, thereby decreasing the soot and carbon monoxide emissions. Recently, Lin et al [26] developed a OME_x-toulene reference fuel (TRF) mechanism that was used for numerical simulations in both HCCI and light duty DICI engine conditions, confirming a a decrease of soot formation when adding OME_x in diesel.

Considering all the above mentioned, a high interest on OME_x as an alternative fuel is justified, for reducing the soot-NO_x trade off as well as the carbon footprint of transport sector. Therefore, the aim of this work is to deepen into understanding how the properties and the molecular structure of OME_x affect the combustion process and pollutant formation of OME_x- fossil diesel blends in a CI engine when the composition is varied within a wide range (from 10 to 50% of OME_x content in the mixture. For this purpose, primarily a direct comparison of different reaction mechanisms from literature was carried out to identify the one that best reproduced the experimental behavior observed. Then, a detailed 3D numerical study of a CI medium duty optical engine fueled with those OME_x–fossil diesel blends was performed. This thesis comprises of the following sections: The first section describes the development of the CFD model; the second one applies the CFD model to investigate the effect of fuel composition on combustion and soot formation. Furthermore, the third section describes the development and validations of the reduced mechanism for OME_x that can incorporate all species i.e. OME (2-4) and can be used in future with different PRF/PAH blends to improve the accuracy of CFD model. The final section describes the conclusions and future work needed for the whole study.

2 CFD Model Development

The following section summarizes the methodology including different type of operating conditions, input parameters and CFD sub-models necessary for the development of CFD Model.

2.1 Computational Domain

Simulations have been carried out using a 3D model of a single cylinder optical engine as computational domain using the commercial CFD code CONVERGE CFD [27]. The geometry is based on the General Motor's medium duty Duramax engine platform (0.8L displacement) used in reference experimental study [28]. The main specifications of the engine are listed in Table 1. The computational domain represents the combustion chamber of the engine that is delimited by

the inner piston surface (bowl and squish region), the cylinder liner and the cylinder head plane as shown in Figure 1.

Figure 1: Computational Domain.

Table 1: Main parameters of the optical engine.

Number of cylinders	1
Bore (mm)	103
Stroke (mm)	99
Displacement (cm^3)	825
Connecting rod length (mm)	163.63
Compression ratio	13.05:1
Engine speed (rpm)	1250
Initial swirl ratio	1.5
Intake valve closing timing ($^\circ$aTDC)	-148
Exhaust valve opening timing ($^\circ$aTDC)	115.5

2.2 Operating Conditions

The simulation was run from inlet valve closing (IVC) to exhaust valve opening (EVO). Thus, only compression, combustion and expansion processes were simulated while air management was excluded. An initial swirl ratio of 1.5 was defined to take into account the air movement at IVC. Thermodynamic conditions used to initialize pressure and temperature fields in simulations were obtained from the experimental measurements in the optical engine used here as reference [28]. For this purpose, an in house developed zero-dimensional single zone thermodynamic model [29] was utilized named as CALMEC. Based on the intake, exhaust and in-cylinder pressures as well as the intake temperature and air mass flow rate, the model is able to calculate in-cylinder thermodynamic conditions at IVC which are later used to define an initial pressure and temperature homogeneous field within the computational domain. The same model was also used to calculate in-cylinder surface temperatures. It uses a nodal model to calculate the liner, piston and the head mean temperatures, which were later used as the boundary conditions for

Table 2: Different Mesh parameters used in Mesh sensitivity analysis.

Mesh Type	Mesh A	Mesh B	Mesh C	Mesh D
Base grid size (mm)	2.0	1.5	1.25	1.15
Mesh size around nozzle [Fixed embedding] (mm)	0.5	0.375	0.3125	0.2875
Total number of cells without embedding and AMR	111664	264685 (+137%)	457376 (+310%)	587367 (+426%)
Computational time	18.5 h	30.5 h (+64.3 %)	36 h (+91.9 %)	38.5 h (+106 %)

the CFD model. Blowby and combustion chamber deformations were not taken into account while fitting the CALMEC model and several trials were done in order to achieve the optimum compression ratio. In order to confirm the accuracy of IVC conditions used for the CFD model, the simulation was first run for the motored (no combustion) case. The Figure 2 (a) shows the in-cylinder pressure comparison between CFD and experimental data between -20 to 20 °aTDC; injection and combustion takes place within this range. The Figure 2 (b) represents the in-cylinder temperature evolution comparison. By looking at both pressure and temperature comparisons, it can be seen that simulation was able to simulate the in-cylinder conditions with accuracy.
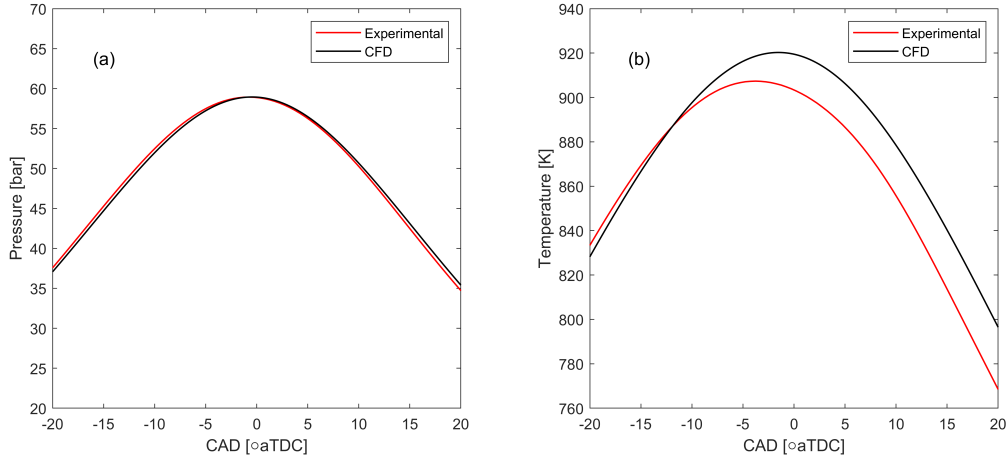
Figure 2: Numerical and experimental in-cylinder pressure evolution (a) and temperature evolution (b) in motored conditions.

2.3 Mesh Configuration

Before selecting an appropriate mesh size, a mesh sensitivity analysis was performed. It's effect over the heat release rate (HRR) and pressure were used as reference. The basic configuration included a fixed embedding scale of 2 around the nozzles as well as adaptive mesh refinement (AMR). It allowed to automatically refine the grid based on local fluctuations of temperature and velocity with a maximum configured embedding scale of 3. The Table 2 shows the different mesh configurations evaluated, where the main parameter modified was the base grid size.

The results of the mesh sensitivity analysis are shown in Figure 3. Data corresponds to the simulation of a blend of 50% Diesel and 50% OME$_3$ (in mass). It can be seen that HRR and pressure are different for the Mesh A when compared to the others, which are much more similar

among them. However, with Mesh B still some small discrepancies in comparison to Mesh C and Mesh D are observed. Therefore, it can was concluded that results were almost not affected by the base mesh size when it was lower than 1.5 mm.
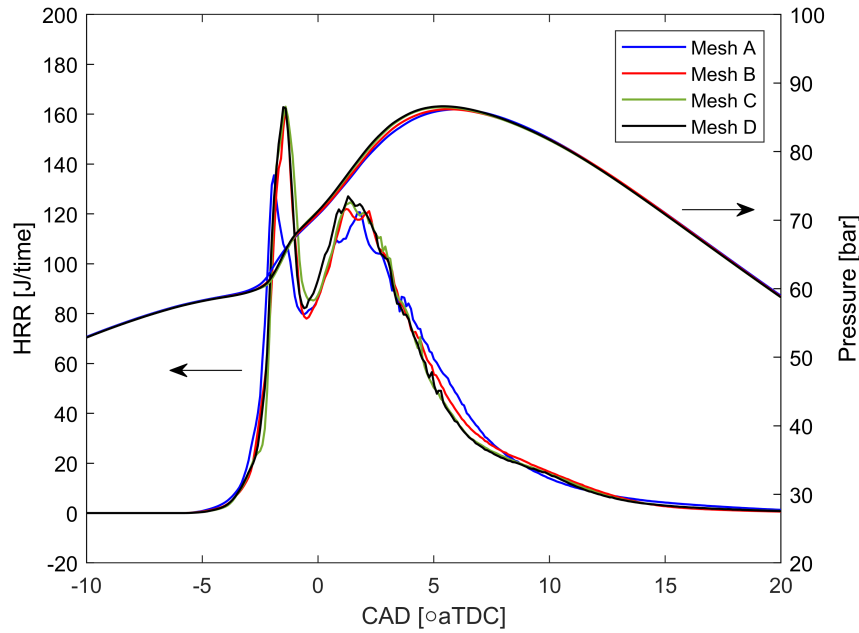
Figure 3: Mesh Sensitivity check for the case of blend of 50%Diesel and 50%OME$_3$.

Considering this, a base mesh size of 1.25 mm with the fixed embedding and AMR previously described, leading to a minimum grid size of 0.3125 mm. The Figure 4 shows the mesh within a plane that represents half of the computational domain at $0°$aTDC. It is possible to see the effect of AMR and fixed embedding around one of the fuel sprays as well as at some regions close to the walls.
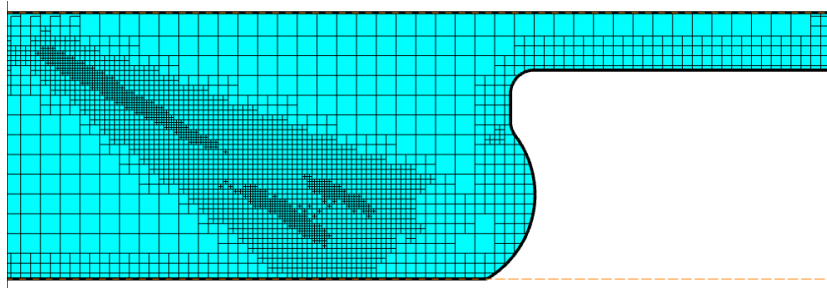
Figure 4: Mesh distribution at $0°$aTDC.

2.4 Chemical Mechanism Configuration

In this study, different blends of diesel with 10%, 20%, 30% and 50% in mass of OME$_x$ were simulated. From here on they will be identified as D90O10, D80O20, D70O30 and D50O50 respectively. However, due to the complexity of this fuels, surrogates ones were used for simulations instead. For diesel, n-heptane was used as it is a widely accepted as a surrogate for conventional Diesel [30][31]. For OME$_x$, it must be taken into account that in experiments the fuel was a mixture

of different OME chains where x varied from 1 to 6. However, only OME_3 (DMM_3) was used as surrogate in this work. The main reasons for using only one fraction of its composition are two. First, the reaction mechanisms that can be found in literature for this type of fuel blended with others only contains OME_x reaction pathways. Second, this fraction was of the largest one in the OME_x that was used in the reference experimental study [28]. Four different reaction mechanisms for the Diesel-OME_x blends were tested in this work. Their main characteristics are summarized in Table 3.

The first mechanism is the one proposed by He et al. [32]. It is a reduced multicomponent mechanism that was developed for oxygenated wide distillation fuel (WDF) with OME_x. It covers surrogate fuels like n-heptane, iso-octane, OME_3 etc. This mechanism has been previously validated against experimentation in a rapid compression machine, homogeneous charge and direct injection compression ignition (HCCI and DICI) engines. The second mechanism was presented by Ren et al. [24]. It is a reduced primary reference fuel (PRF)-OME_x chemical mechanism and has been extensively validated in a HCCI engine. The third mechanism considered in this study is a (PRF)-OME_x compact mechanism, proposed by Lin et al. [33] and extensively validated against a wide range of experimental data. The fourth and last mechanism was recently published by the same authors [26]. The main difference with the previous one is that it is a toluene reference fuel (TRF)-OME_x mechanism that contains TRF-polycyclic aromatic hydrocarbons (PAH) chemistry, essential for soot predictions. It has also been validated against a range of experimental and simulation results.

Table 3: Overview of reaction mechanisms used.

Mechanisms	Number of species	Number of reactions	Mechanism type
He 2017 [32]	354	943	WRF-$PODE_n$
Ren 2019 [24]	145	585	PRF-$PODE_n$
Lin 2019 [33]	61	190	PRF-$PODE_3$
Lin 2021 [26]	120	360	TRF-$PODE_3$

2.5 Injector Configuration

In this simulation, an injector with 8-hole nozzle was used. The start of energizing (SOE) was set at $-9°$aTDC for every case with a start of injection (SOI) delayed about 2.196 CAD from SOE and a total injection duration of $8.685°$ as it was measured experimentally. The discharge coefficient was kept constant at 0.9 with the orifice diameter of 135 μm. The angle between the cylinder head plane and the spray axis (-zx plane) was set to $60°$ as it was experimentally measured where an in-house procedure was utilized to obtain certain parameters such as distance between two spray impingements, distance from nozzle center to spray impingement point etc. while measuring and then MATLAB script was utilized to accurately get the angle . The spray cone angle was set to be $14°$ as obtained by using a correlation from [34], where this parameter is calculated by an empirically derived equation for a vaporizing spray using the values of the ambient gas density, ambient fuel density and a constant equal to 0.26. Main spray injection parameters used are shown in the Table 4 below.

Table 4: Main injection spray parameters.

Start of Energizing (SOE)(°aTDC)	-9
Start of Injection (SOI)(°aTDC)	-6.804
Injection duration (°)	8.685
Injection profile	Single main injection
Injection Pressure (bar)	1000
Number of nozzles	1
Number of holes in nozzle	8
Discharge co-efficient	0.9
Orifice diameter (μm)	135
Spray cone angle (°)	14
Angle between spray axis and cylinder head (-zx plane)(°)	60
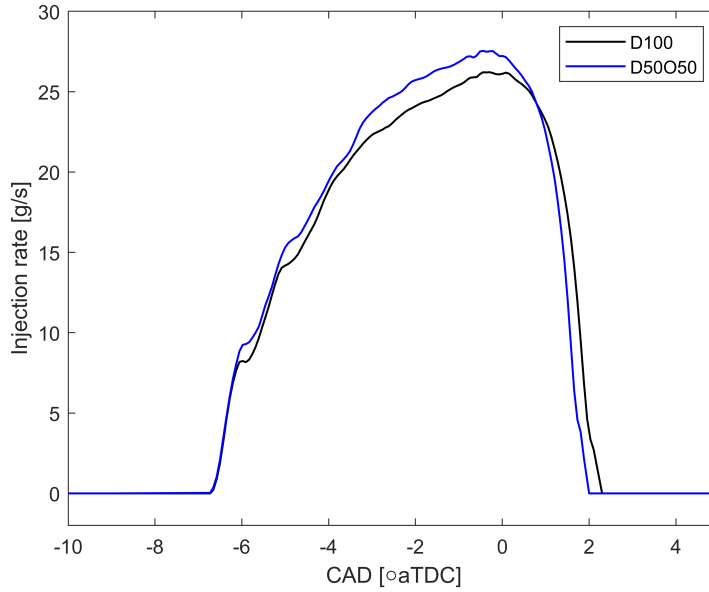
Figure 5: Mass flow rate for D100 and D50O50 case.

The injected mass flow rate was experimentally measured for D100 (corresponding to 100% pure diesel) and D50050 at 1000 bar injection pressure with the energizing pulse of 900 μs, as in reference experiments, following the methodology described in [28]. Both injection rate profiles have been presented in Figure 5.

As it can be observed, the main effects when increasing the OME_x content is that the instantaneous mass flow rate increased while its duration was slightly shortened (2% of total duration). These resulted in a noticeable increase of the total injected mass when increasing the OME_x content. For sake of simplification, it was decided to use the D50O50 normalized injection rate profile for all the fuels. However, to take into account the described behaviour, the corresponding measured total injected mass was used for D50O50 while a different value was calculated for D90O10, D80O20 and D70O30 (as no measured values were available). For this purpose, a linear relation between OME_x content and total injected mass variation was assumed and the values corresponding to 10%, 20% and 30% of this fuel were calculated using a linear interpolation procedure. The

total injected mass calculated for each fuel is summarized in Table 5.

Table 5: Injected mass for each blended fuel.

Blend	Total injected mass (mg)
D50O50	32.22
D70O30	31.44
D80O20	31.05
D90O10	30.66

2.6 Spray, Turbulence, Heat Transfer and Combustion Models Configuration

In CI engines, the liquid fuel is injected near the end of compression stroke inside the combustion chamber. So, after injection, the fuel spray undergoes numerous processes like atomization, vaporization etc. There are numerous models available for each phenomenon in the CONVERGE CFD library to handle these phenomena. The Table 6 shows a summary of the ones used in this work.

Table 6: Different Spray Models used.

Liquid Injection	Blob Injection
Spray breakup	Modified KH-RT
Drop Drag	Dynamic Drag Model
Collision Outcome models	Post collision outcome
Turbulent dispersion	O'Rourke model
Collision Model	No time counter (NTC) collision
Spray/wall interaction model	Rebound/slide

The liquid injection model employed here was blob injection model [27] that simply depicts the parcels that are injected inside the computational domain with a characteristic size equal to the size of the nozzle diameter. The spray model used here is based on lagrangian drop eulerian type and the modified Kelvin-Helmholtz Rayleigh-Taylor (Modified KH-RT) was used as a spray breakup model [27]. In this model the primary breakup of injected liquid blobs is due to the aerodynamic instabilities. During this process child drops are formed and the secondary breakup of these drops is modelled by assessing the competing effects of KH and RT Mechanisms. The droplet collision was based on No time counter (NTC) model by Schmitz and Rutland [27]. This method involves the randomly determined sub sampling of the parcels within each cell that results in much faster collision calculations. Finally, a rebound/slide model was used to model the spray wall interaction. All these spray models described are well used in literature and are recommended by CONVERGE for diesel engine simulations.

The Re-normalization group (RNG) k-epsilon was used to resolve turbulence, with a standard wall function. The renormalized model is more robust than the standard k-epsilon. The effect of turbulence interaction and spray compressibility is included in this model. Turbulent kinetic energy and turbulent dissipation values were provided accordingly. The heat transfer in this simulation was modelled by O'Rourke and Amsden [35][36] model as it is recomended for

diesel engine applications. Although, all the other models namely Han and Reitz, Angelberger, GruMo-UniMORE were also tested but the O'Rourke best fitted the experimentally obtained heat transfer through combustion chamber walls obtained through CALMEC. The Figure 6 depicts the comparison between different heat transfer models implementation in simulation. O'Rourke and Amsden was used in the end in further simulations as it is most recommended for diesel engine applications [27].
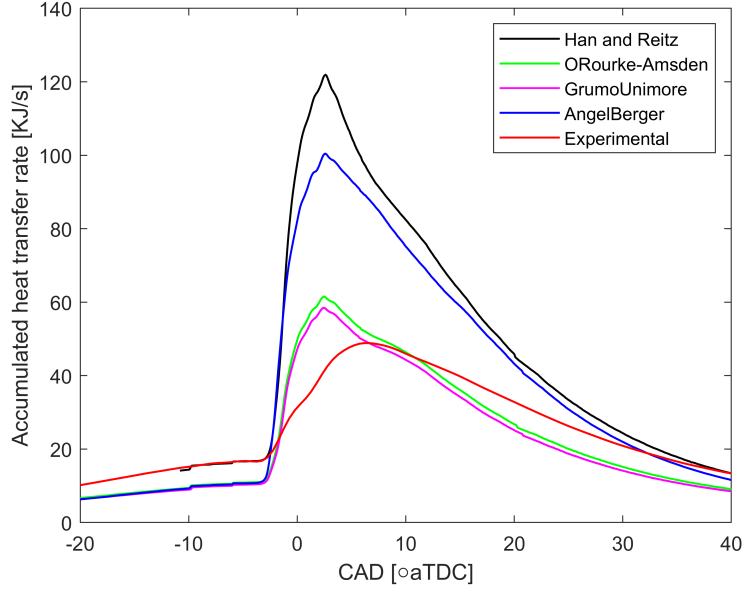
Figure 6: Accumulated heat transfer through combustion chamber (piston, cylinder walls, cylinder head) by using different heat transfer models

Navier stokes solver scheme PISO [37] i.e., pressure implicit with splitting of operators, density-based scheme was utilized. Besides, variable time-step scheme was used, that describes each time-step within a pre-defined interval (from $1\cdot10^{-8}$ to $1\cdot10^{-4}$) based on the maximum number of iterations allowed for the governing equations and the iterative solver, the maximum Courant-Friedrichs-Lewy (CFL) numbers and other restrictions related with sub-models like the spray model [27].

Regarding the combustion modelling, CONVERGE contains a detailed chemistry solver named SAGE [38] that solves the detailed chemical kinetic through the CHEMKIN formatted input files on each computational cell. SAGE solver calculates the elementary reaction rate while CONVERGE solves the transport equations. It happens to provide accurate results in terms of diesel combustion. Moreover, Hiroysou soot model was used in terms of soot modelling in this study.

3 Evaluation of CFD Model & its Application: Effect of Fuel Composition on Soot Formation

The following section summarizes the results, evaluation and discussions related to the above developed CFD model for Diesel-OME$_3$ simulations.

3.1 Evaluation of Reaction Mechanisms

Discussion starts by evaluating the comparison of the different reaction mechanisms considered in this study. For this purpose, HRR and in-cylinder pressure signal for D50O50 have been compared with the reference experimental data.
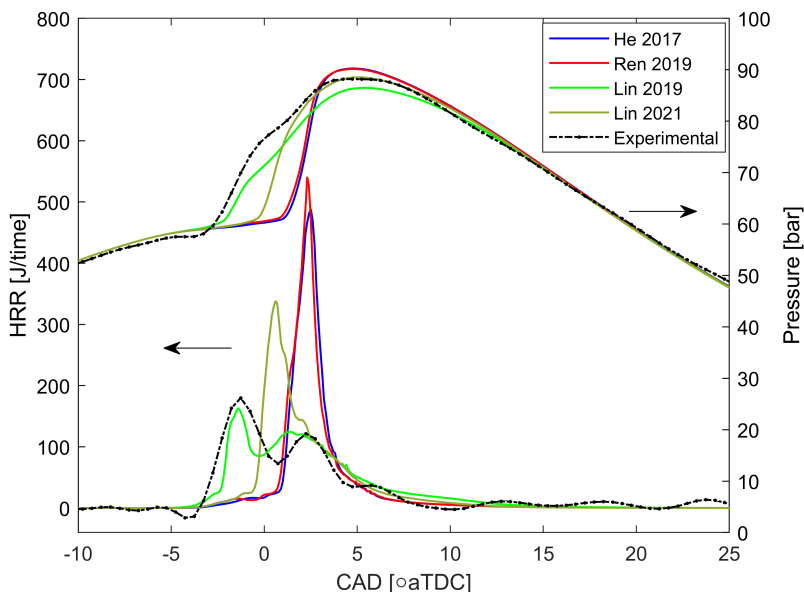
Figure 7: Experimental data and different mechanisms simulations (CFD) of pressure profile and heat release rate for D50O50.

The Figure 7 shows the HRR and pressure curves obtained by using the four mechanisms and their comparison with the experimentally obtained curves. It is possible to see that only one of the four mechanisms was able to predict a similar behaviour as of experimental data, which is the compact mechanism provided by Lin et al. [33]. It is able to reproduce a similar ignition delay as well as premixed and diffusion phases of the experiments. The longer mechanisms in terms of number of reactions, i.e. [32][24], show a quite similar behaviour between themselves. They predict a longer ignition delay than experiments which results in a more intense premixed phase and almost no diffusion. The mechanism provided by Lin et al. [26] in 2021 also exhibits a longer ignition delay with a more intense premixed phase than experiments. The accuracy on reproducing ignition delay by the Lin 2019 mechanism [33] was also observed by Hovden et al. [39], where the authors performed 0D simulations in a constant volume reactor for ignition delay calculations. Thus, this mechanism was chosen to carry out further simulations in this study.

3.2 Effect of Fuel Composition on Combustion Performance and Energy Release

When analysing the effect of the blend composition on the combustion process development, differences start to appear since the start of combustion. The Figure 8 shows the ignition delay (ID) obtained both from experimental data and numerical simulations. It has been calculated as the delay between the SOI and the first instant when the HRR goes above 0. It is possible to see that ID slightly increases when OME_x content in blend is decreased. Despite the difference of $2°$

between both data sources, it can be stated that the trend obtained with the numerical simulations regarding the fuel composition is corroborated by experiments. This behaviour could be related with the fact that as OME_x content is decreased in blend, the oxygen supplied by the fuel itself also decreases making the blend less reactive and delaying combustion. However, the relation between ID variation and OME_x content is not linear. Above 20%, ID tends asymptotically to a value close to that shown by D50O50, which suggest that for such blends the most reactive component (OME_x) is controlling the start of combustion [40] and diesel has almost no influence. The same trend can be observed in experiments except for D50O50, which will be analysed in more detail in the following paragraphs.
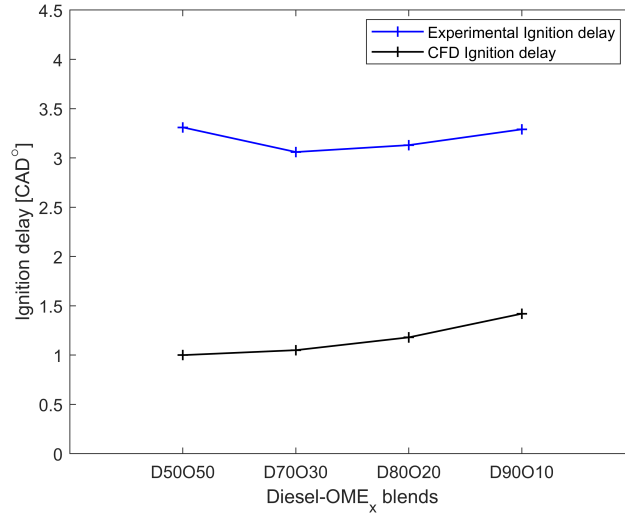
Figure 8: Both experimental and CFD ignition delay.

The results obtained with the selected mechanism for the four blends related to the in-cylinder heat release rate and pressure evolution are compared in Figure 9. In general, numerical simulations are able to predict similar trends as those observed in experiments. However, it is important to mention that experimental D5050 deviates from them showing a similar energy release as D90O10 (and also a ID higher than expected). This has been related to experimental errors since this behaviour can not be explained by the fuel properties. When comparing the different blends, the effect of its composition starts to be visible when the premixed combustion phase is taking place (between -3° and 0° aTDC). The HRR maximum peak decreases when increasing the OME_x content in the blend. On one hand, this can be related to the fact that the LHV of this fuel is lower than that of pure diesel and, therefore, the energy released by each blend at this stage will be different. In this sense, the increase in the injected mass previously reported seems to not be enough to compensate the energy difference. On the other hand, the ID has an impact on the amount of fuel that mixes with air before combustion and, as a consequence, the energy released in the premixed phase. Thus, the higher ID observed when decreasing the OME_x content is coherent with the more intense HRR peak observed in both CFD and experimental data. Moving further into the diffusion stage, it can be observed that all the fuels present a similar HRR. However, after 5° aTDC the decrease of energy release is more abrupt for the blends with higher OME_x content. This is especially visible when comparing D50O50 and D70O30 with the other two blends and suggest a faster late oxidation stage. This behaviour is clearly visible for the numerical simulation results and is corroborated by experiments, despite the larger oscillations the discrepancies

13

observed for D50O50 as it was previously mentioned.
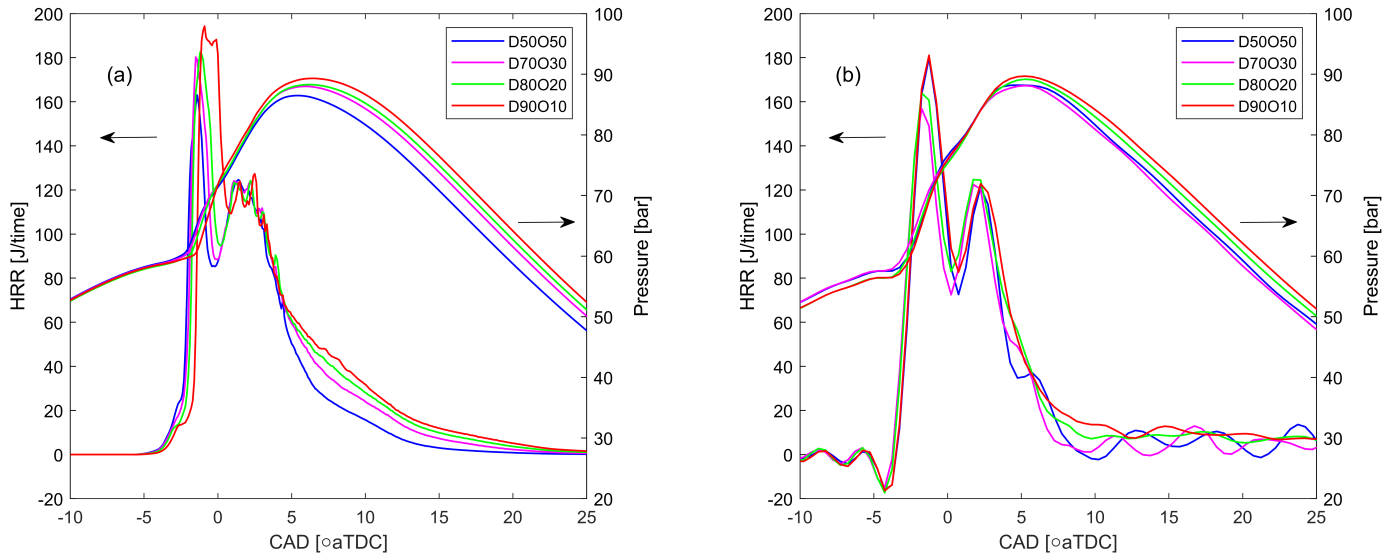
Figure 9: In-cylinder pressure and heat release rate obtained from numerical simulations (a) and from experimental results reproduced from [28] (b).

At this point, a strategy was defined to quantify how fast combustion is progressing with each blend with respect to D90O10, chosen as reference. The fraction of energy released at $15°$aTDC from the total energy released at the end of combustion was calculated, to evaluate how far combustion was completed . This instant was chosen as reference, since it corresponds to the late stages of combustion.
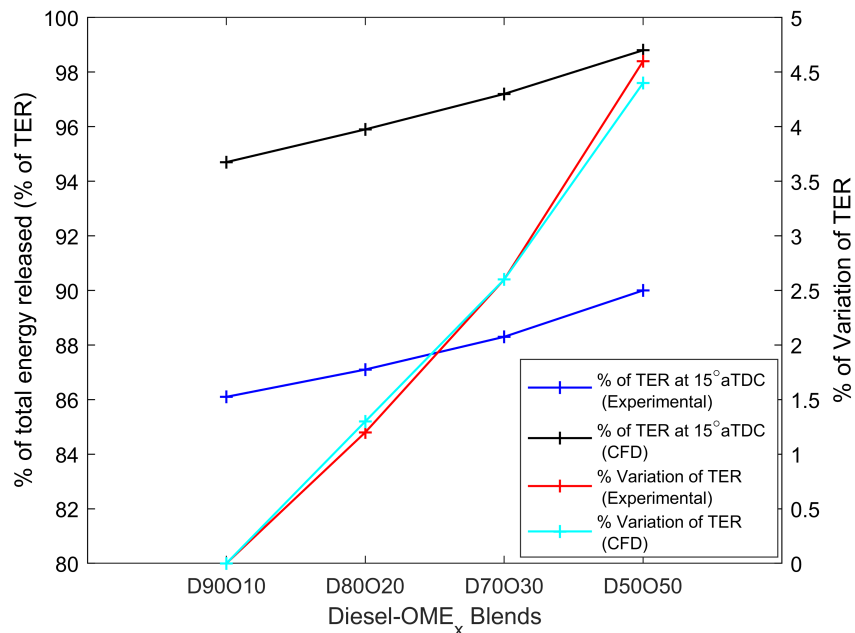
Figure 10: Numerical vs experimental percentage of total energy released (TER) at $15°$aTDC for each blend and the percentage variation of this parameter w.r.t D90O10 results.

14

The Figure 10 shows a comparison of the experimental and numerical data, including the percentage of total energy released (TER) for each fuel at $15°$aTDC as well as the percentage of its variation with respect to the reference case (D90O10). It can be seen that the percentage of energy released is higher for the case of the largest OME_x fraction and decreases when OME_x fraction is decreased. In fact, by looking at the percentage of variation, D50O50 combustion is almost 5% more complete at $15°$aTDC than D90O10. It can be also observed that the trend obtained with CFD is again corroborated by experimental data. Therefore, it can be concluded that combustion is accelerated when increasing the OME_x fraction in the blend.

3.3 Equivalence ratio, Temperature and OH distributions

One of the main differences of OME_x when compared to fossil diesel is its molecular composition, which will affect the stoichiometry of the air/fuel mixture and will have an impact on the combustion process. Thus, to get a deeper insight into stoichiometry of the blends, the spatial distribution of equivalence ratio (Φ) inside the combustion chamber is shown in Figure 11.
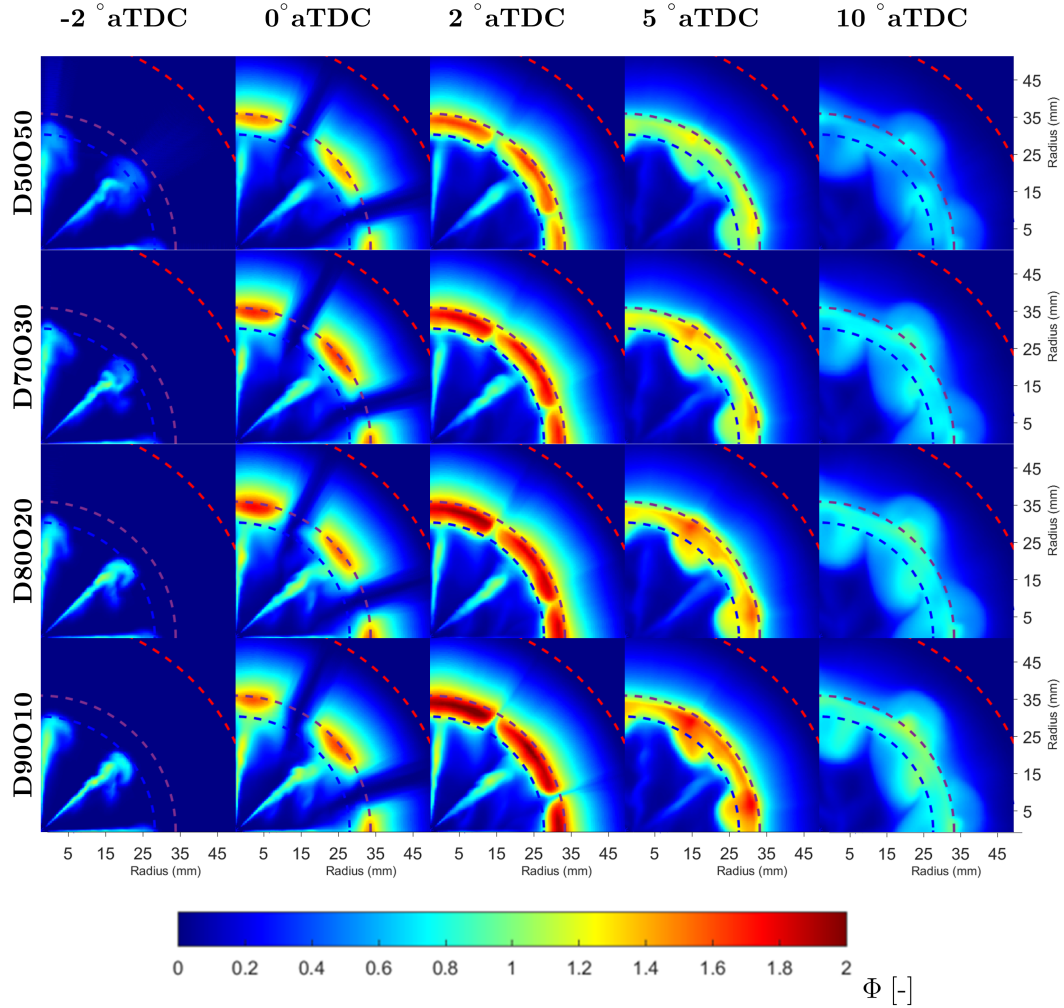
Figure 11: Average equivalence ratio distribution inside the combustion chamber for the four blends. Data corresponds to numerical simulations.

The data corresponds to the average equivalence ratio calculated between the piston and cylinder head. Besides, it is worth mentioning that Φ in this case do not consider CO_2 and H_2O. It is preferred in this case over the overall equivalence ratio because it can be related with the progress of the reaction [27]. The inner dotted line in the figure represents the field of view of experimental OH* chemiluminescence visualization presented in [28], the middle one represents the bowl radius and outer line represents the piston radius. Besides, it has been decided to represent only a quarter of the bowl to match the experimental data available in [28].

In the figure it is possible to see that higher Φ values are located at the periphery of the bowl for all the cases. In general, D50O50 shows lower equivalence ratios than the other blends. In fact, it is possible to see that the more the OME_x is in the blend, the lesser equivalence ratios obtained. At $2°$aTDC (the beginning of the diffusion stage), all the blends seem to reach equivalence ratio values above 2, which decrease as the combustion progresses. At $5°$aTDC, the differences among blends are significant with D50O50 showing large regions where equivalence ratio was below 1. In contrast, D80O20 and D90O10 still show regions where Φ is close or even above 2. According to Kitamura et al. [41], more soot is likely to be formed in the regions where Φ is higher than 2. So, based on this, it can be expected that the lower Φ fields achieved thanks to the OME_x content in the blend would result in less soot formation.
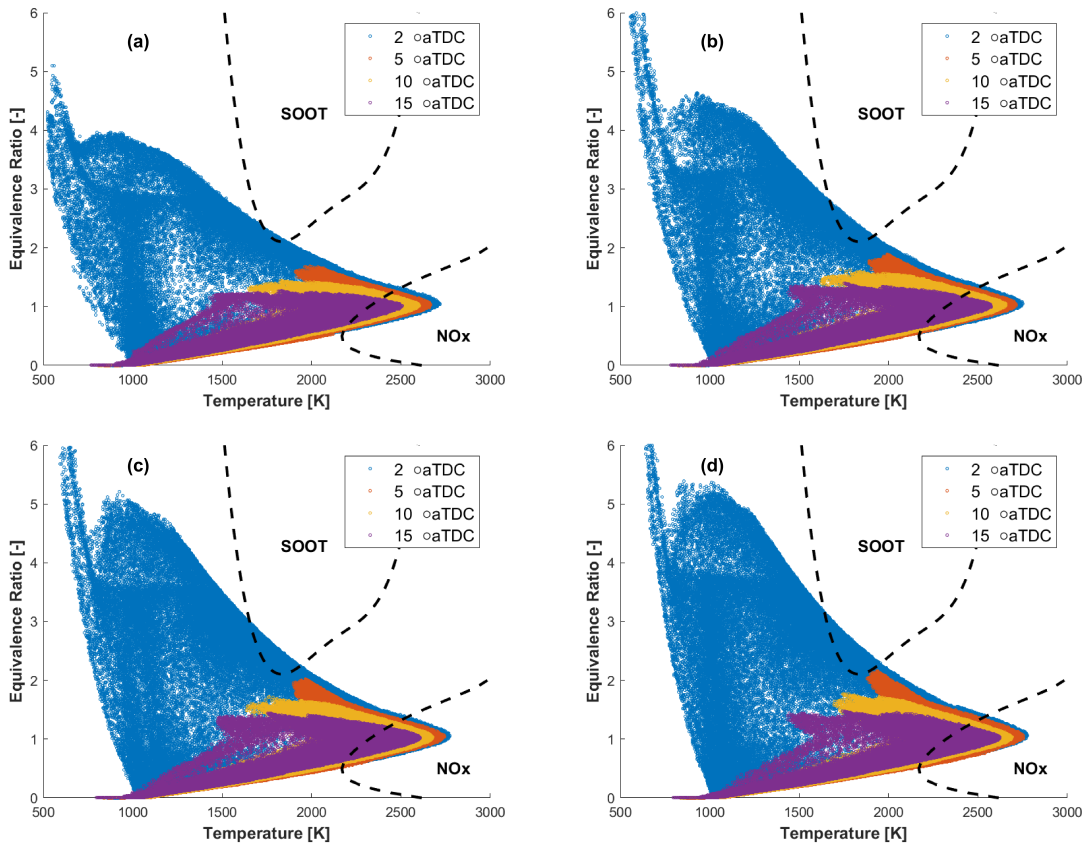
Figure 12: Equivalence ratio vs temperature distribution for D50O50 (a), D70O30 (b), D80O20 (c) and D90O10 (d) at different instants. Data corresponds to numerical simulations.

The Figure 12 represents the Φ-temperature diagrams for all the blends at different CAD's.

Each point corresponds to one of the cells of the computational domain while the dashed lines represents the soot and NO_x peninsulas. Notice that only at 2°aTDC points in the soot peninsula are visible for every case, with D90O10 showing more points in this region than the other blends. This indicates that soot is likely to be formed at around 2°aTDC and the difference is when decreasing the OME_x content as the point cloud seems to be progressively leaving the soot peninsula. When looking at later instants, it is possible to see that an increase of the oxygenated fraction reduces the Φ field. For example, when looking at the 5°aTDC case, it can be observed that D50O50 is not reaching Φ values above 1, while D90O10 exceeds 2. Regarding temperature, it seems that differences are minimum although it has been reported in [25] that the more OME_x content in the blend, the lesser the equivalence ratios (also observed in this work), but the higher the in-cylinder temperature reached.

The OH radical is considered as a good tracer of high-temperature oxidation reactions. Its spatial distribution identifies the regions where oxidation is taking place. For this reason, it has been decided to investigate the evolution of this radical. In a first approach, the Figure 13 (a) represents the accumulated OH mass inside the combustion chamber obtained by CFD for each blend. This data should be comparable with the OH* accumulated intensity in Figure 13 (b) presented by Pastor et al. [28].
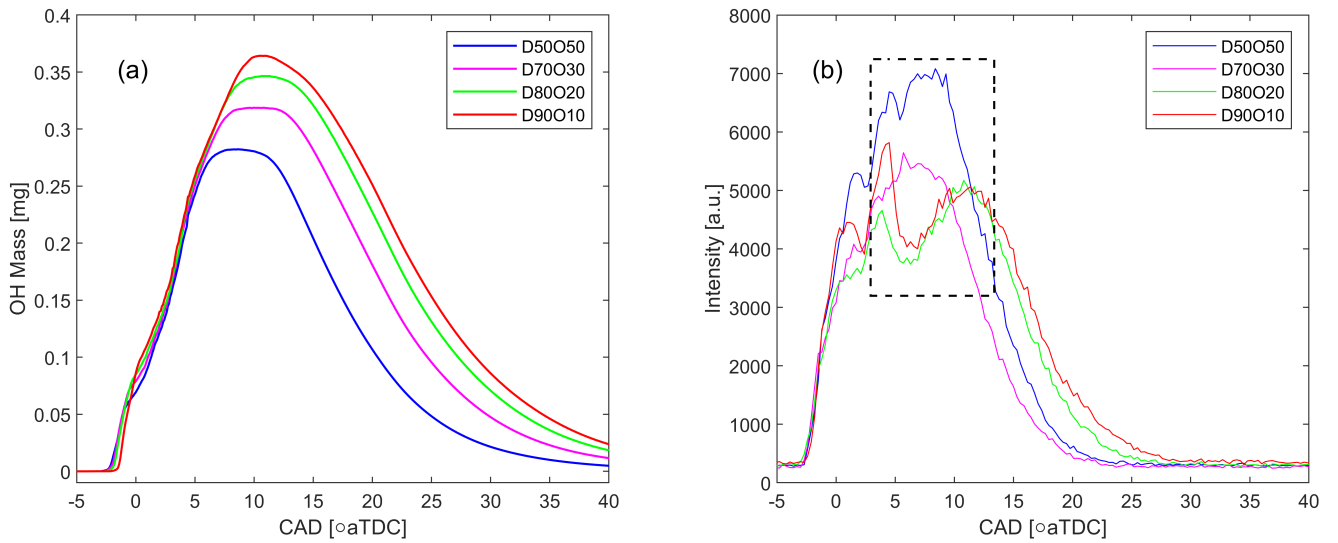
Figure 13: In-cylinder accumulated OH mass from numerical simulations (a) and experimental accumulated OH* radiation (b) for all the blends.

It is possible to see that until 5°aTDC all the fuels provide a similar amount of OH mass which is corroborated by the OH* radiation. However, differences appear after 5°aTDC when a decrease of the OME_x content in the blend results in an increase of the in-cylinder OH mass. This is observable with the CFD data but not with experiments. In fact, until 15°aTDC, the second source shows a different trend. However, is was stated by the authors of the experimental work that at this stage of combustion (interval delimited by the dotted rectangle) the soot peak was reached and the images were contaminated by soot radiation [28]. The OH content starts decreasing earlier for D50O50 and the lesser content of OME_x in the blend seems to delay it more. This results in a sooner disappearance of OH from the combustion chamber, which is coherent with the faster combustion process that was previously mentioned. After 15°aTDC, experimental

17

data provide again a similar trend among the blends as CFD (once soot radiation is not so intense) showing a sooner decay of the signal when the OME_x content is increased. Only experimental D50O50 shows a different behaviour, which has been already discussed in the previous section.

To analyse in more detail how the OH radical is distributed within the combustion chamber, the Figure 14 represents the spatial distribution of this radical obtained with numerical simulations. The represented data corresponds to the accumulated OH mass between the piston and the head surfaces, for all the blends at different instants. Notice that here again only a quarter of the combustion chamber has been represented to match the field of view reported in [28]. The inner dashed line represents the limit of the field of view of the OH* chemiluminescence experimental visualization, the middle dashed line represents the piston bowl radius and the outer dashed line represents the piston radius.
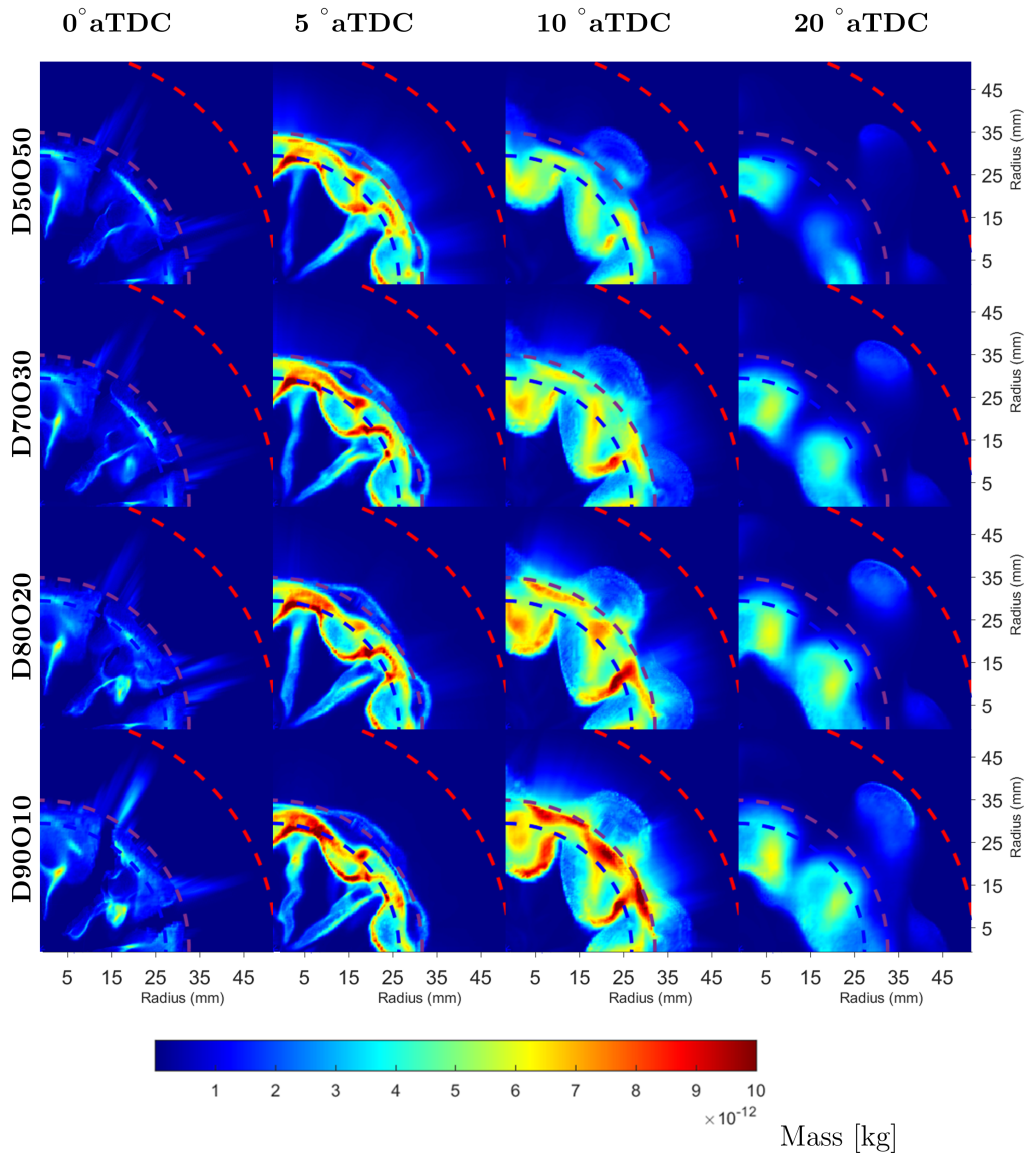
Figure 14: Accumulated OH mass inside the combustion chamber. Data corresponds to numerical simulations.

At the first instants, OH seems to be accumulated close to the periphery of the bowl, which was also observed in the OH* chemiluminescence images from [28]. Moving further , at $10^°$aTDC significant differences start to appear among blends. D50O50 shows spots of lower OH mass close to the bowl wall while this is not observable for the rest of the blends. Besides, in general the OH field of this blend is lower than the rest. This can be related to the different equivalence ratio distributions reported in Figure 12. Those spots correspond to the regions where Φ was close to 1. The sooner disappearance of OH observed in Figure 13 is also visible here.

At $20^°$aTDC, the major part of OH has disappeared for D50O50 and only small isolated clouds remain. In contrast, the other blends still show larger clouds of higher OH mass which take longer to disappear. For these fuels, the OH clouds seem to evolve from regions where Φ reached the higher values in previous instants, e.g. $5^°$aTDC. However, for D50O50 they seem to evolve from regions where Φ was significantly below 1.

Considering all the above mentioned, there is a relation between the blend composition, the Φ distribution and the OH distribution. The more OME_x in the blend results in a lower Φ field, thanks to its different stoichiometry (the oxygen content). D90O10, D80O20 and D70O30 provided regions of Φ close or higher than 2 even at $5^°$aTDC. However, at this stage for D50O50 Φ is lower and closer to 1. This promotes more oxidation in comparison with the other blends, which result in a faster combustion completion (see Figures 9 and 10) and a sooner OH disappearance.

3.4   Soot Formation

As it has been already mentioned in the previous paragraphs, the different Φ fields obtained by each blend will have an impact on soot formation. To analyse this, Figure 15 shows the net amount of soot formed (a), the amount of soot produced (b), the amount of soot oxidized (c) and its percentage in relation to the total soot produced (d). The net amount of soot formed is the difference between the soot produced and oxidized.

As it can be observed, with the increase of OME_x in the blend, the amount of soot produced decreases while the proportion of soot that is being oxidized increases. This agrees with the Φ-T maps presented in Figure 12, where it was observed that the less OME_x content resulted in a larger number of points within the soot peninsula at $2^°$aTDC. In fact, this is the instant when the soot production starts to increase faster for the blends with the lower OME_x fraction. Later, at $5^°$aTDC, the Φ values decrease (see Figure 12) for all the fuels and the soot production stops and oxidation becomes dominant. The lower Φ field provided by D50O50 allows it to oxidise the soot faster than the other blends as in can be seen in Figure 15 (d). Besides, the results also show that the effectiveness of oxidizing soot increases with the OME_x content which is consistent with the progressive decrease of Φ values observed previously.
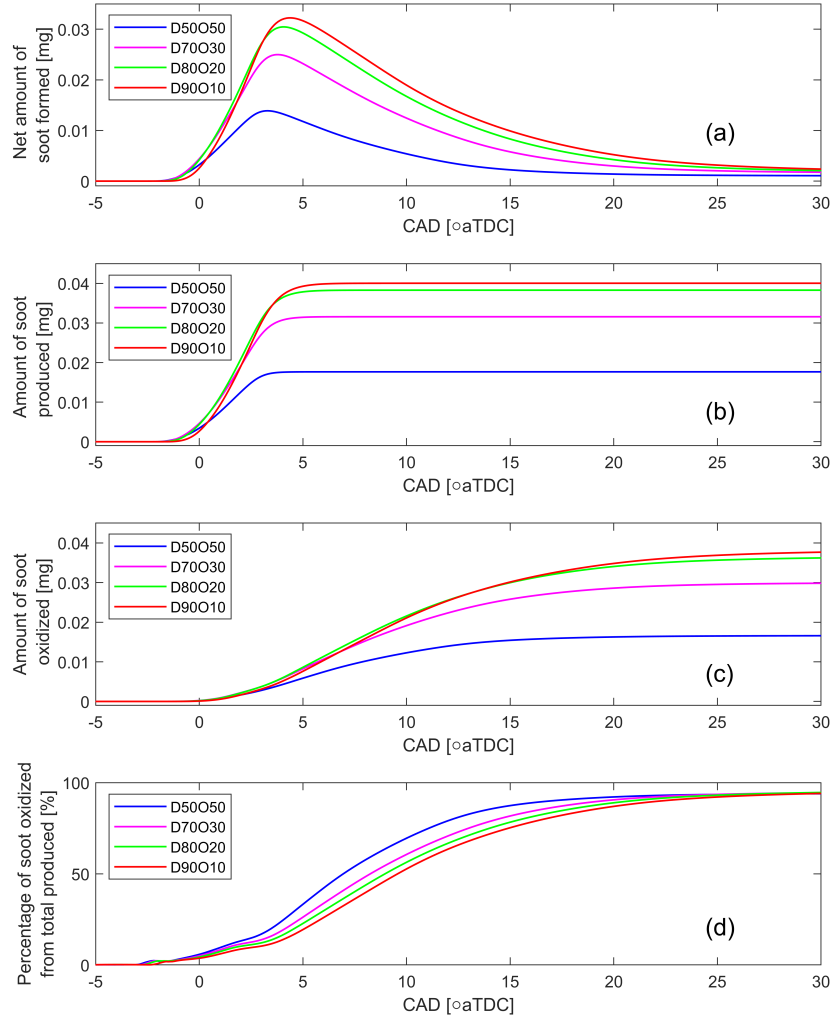
Figure 15: Evolution of the net amount of soot formed (a),the amount of soot produced (b), the amount of soot oxidized (c), and the percentage of soot oxidized from the total produced (d).

The spatial distribution of soot is presented in Figure 16, where the net soot formed inside the combustion chamber is shown. Data corresponds to the accumulation of soot mass between the piston and the head surface. Only a quarter of the combustion chamber has been represented as in Figure 14. These distributions show that at the beginning (close to TDC) the soot distribution is similar for all blends. At 2°aTDC differences appear, as stated previously. In all the cases, soot is mainly formed near the bowl walls which correlates with the experimentally obtained high speed natural luminosity images found in [28]. Besides, it corresponds with the regions of higher Φ values in Figure 11.
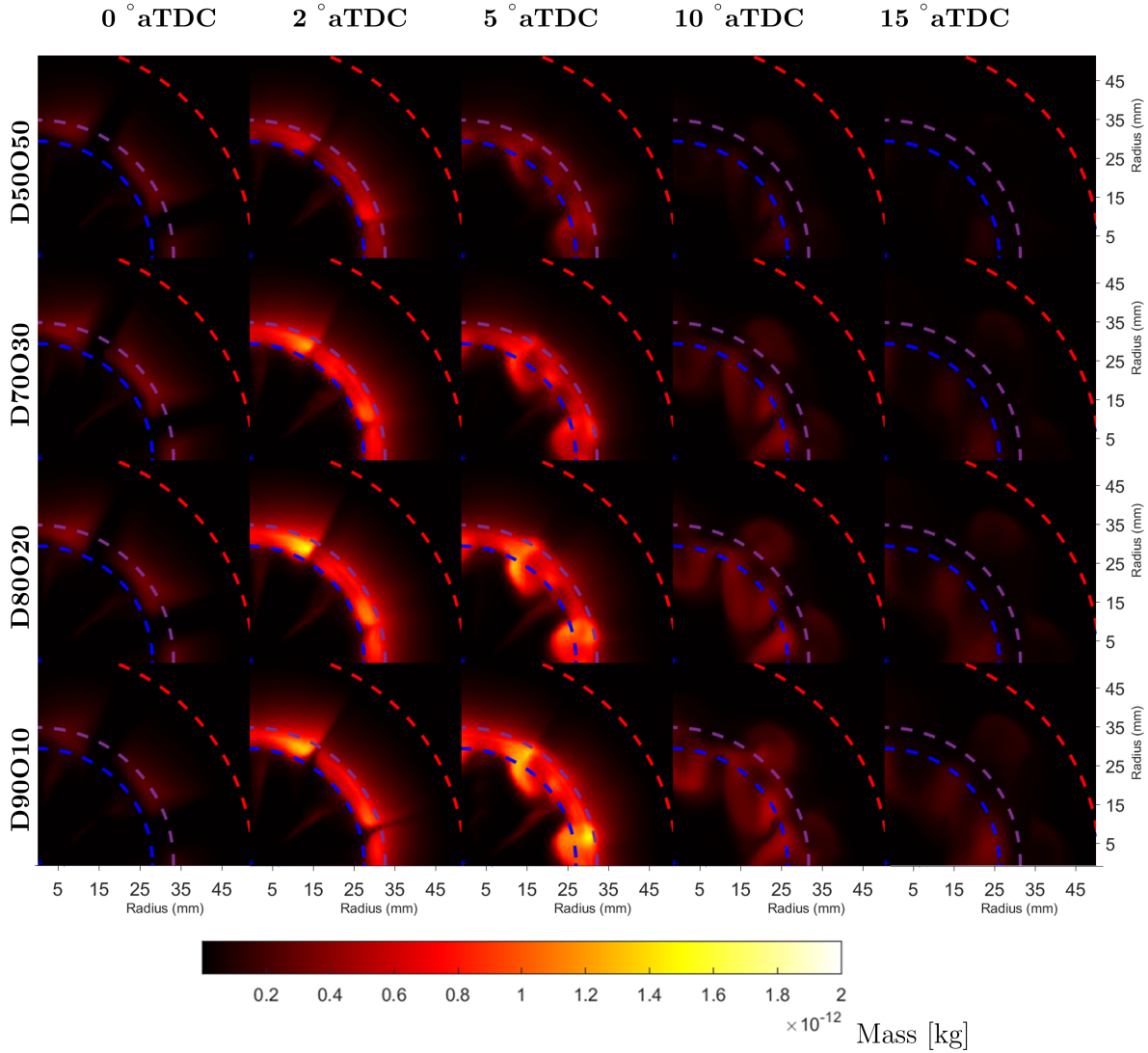
Figure 16: Accumulated soot mass inside the combustion chamber. Data corresponds to numerical simulations.

The differences among blends are then mostly related to the amount of soot but not with its distribution. When combustion progresses, it can be seen for D70O30, D80O20 and D90O30 that soot clouds move towards the piston center while this is not visible for D50O50. This can be related to the fact that, due to the air and spray dynamics, the flames are pushed towards this region. As soot lasts longer when the OME_x content is decreased, these clouds are able to travel longer distances while for the last blend i.e. D50O50 they disappear before the other three blends.

4   Mechanism Reduction

One of the weak points of the previous work is the use of only OME_3 to represent the whole OME_x, whereas OME_x is a mixture of different chains of OME where x ranges from 1 to 6. Hence keeping in mind this aspect of the previous work, it was decided to develop a more detailed mechanism that comprised of OME 2-4. For this purpose, the following section describes the methodology utilized for the reduction.

4.1 Implementation of Reduction Techniques

The detailed OME 2-4 mechanism was taken from an already published and verified work by [42]. This mechanism comprised of 322 species and 1611 reactions. However, this mechanism was too large to keep a reasonable computational cost. From now own it will be referred as master mechanism.

Various different reduction techniques have been used by authors to reduce complex mechanism. Mainly, the reduction process has been carried out in the past by utilizing a commercial software called ANSYS Reaction Workbench which is a part of ANSYS CHEMKIN. This software is specifically developed to perform operations related to chemical mechanism. In [24][25][43] the same software was utilized to reduce complex mechanisms although their technique was different from each other. Main reduction techniques include Direct relation graph (DRG), Direct relation graph with error propagation (DRGEP), Direct relation graph with path flux analysis (DRGPFA), and Sensitivity analysis.

DRG is the simplest of the reduction techniques that is basically utilized to reduce detailed mechanisms by identifying unimportant species in a reaction mechanism without any prior knowledge of the system. DRGEP, is an extension of DRG technique along with error propagation. It basically evaluates the relevance of a reaction relative to other reactions. DRGPFA is considered to be more effective then DRG or DRGEP under certain conditions. It basically works by identifying both production and consumption rection pathways instead of only absolute reaction rate that are used in DRG or DRGEP. As we move from DRG to DRGEP to DRGPFA, the computational cost increases. After utilizing these techniques, sensitivity analysis is performed that basically evaluates the absolute relevance of a reaction. The sequence of implementation of these techniques depends upon the master mechanisms but in the many authors use the same sequence in the past in addition of 1 or 2 additional techniques [24][25][43]. Therefore, in this work a similar sequence has been utilized, which is shown in Figure 17. Starting from DRGEP, DRGPFA is applied and then in the ending stages sensitivity analysis is utilized alongside DRGEP.
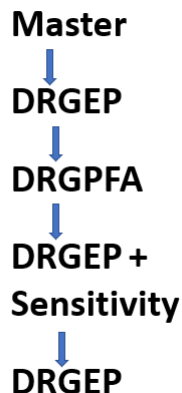
Figure 17: Reduction techniques sequence.

4.2 Fuel Composition and Operating Conditions

The composition of the fuel chosen for the reduction of the mechanism consisted of (0.97% OME2 + 57.62% OME3 + 41.4% OME4). The reason for using this specific composition was to match the one corresponding to the already available experimental data of OME 2-4. A set of same operating conditions were identified from [42] (master mechanism) and were utilized in the reduction process. The table summarizes a set of different pressures, temperature and equivalence ratio range used.

Table 7: Input conditions matrix for reduction.

Temperature (K)	650-1150
Pressure (bar)	10,20
Equivalence ratio (-)	0.5,1.0,2.0

Besides a tolerance of 1 microsecond for ignition delay validation was chosen as a primary

parameter for reduction and a different set of species were retained inside the reduced mechanisms like OH, CH_2O, C_2H_2 etc.

4.3 Results and Validation

The implementation of the above discussed sequence of reduction techniques and the operating conditions resulted in a reduced mechanism consisting only of 159 species and 693 reactions. A summary of step-by-step reduction process is shown in Figure 18. It is clear that the DRGEP and DRGPFA technique was much effective in reducing the mechanism while sensitivity analysis seemed to only optimize the already reduced mechanism.

- Master: Contained **322 species and 1611 reactions**
- DRGEP: Reduced to 217 species
- DRGPFA: Reduced to 184 species
- DRGEP + Sensitivity: Reduced to 161 species
- DRGEP: Reduced to 159 species
- Reduced mechanism contains **159 species & 693 reaction**

Figure 18: Summary of reduction techniques results.

A variety of validations have been carried out while performing the mechanism reduction. These validations include mainly ignition delay, laminar flame speed, species concentration and in some cases a 3D CFD validations were also performed by different authors [32][33][43][26]. Considering the literature review, validation techniques were applied in this work as described below.

4.3.1 Ignition Delay

Autoignition and combustion characteristics of target fuels can be evaluated from ignition delay times, which play a significant role in advanced combustion mode research and engine-out emission reduction. The reduced OME_x mechanism should perform well for each neat fuel component. Ignition delay simulations were performed in a 0D closed homogeneous reactor over a wide range of input conditions as highlighted above. As it can be seen in Figure 19 the reduced mechanism performs quite well in comparison to master mechanism.

Further, validations of individual fuel components were also performed which highlighted some differences regarding OME_2, the reason was that the mole fraction used for OME_2 in the reduction was too small i.e., 0.97%. The Figure 20 shows data for individual fuel components at 20 bar with equivalence ratio of 1. OME_2 differences are clearly visible. In terms of OME_3 and OME_4, the mechanism worked well both at low and high temperatures. It must be considered that the differences observed for this two components with the experimental data are similar to those offered also by the master mechanism.
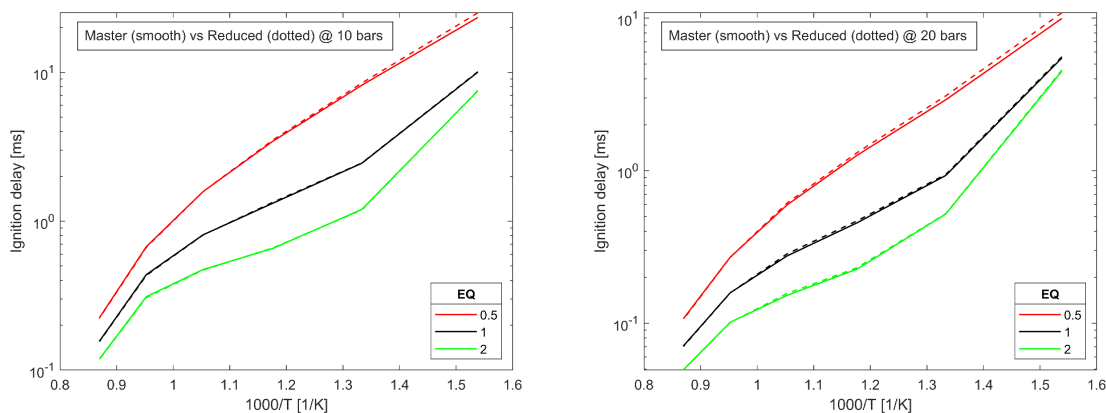
Figure 19: Ignition delay comparison between master and reduced mechanism.
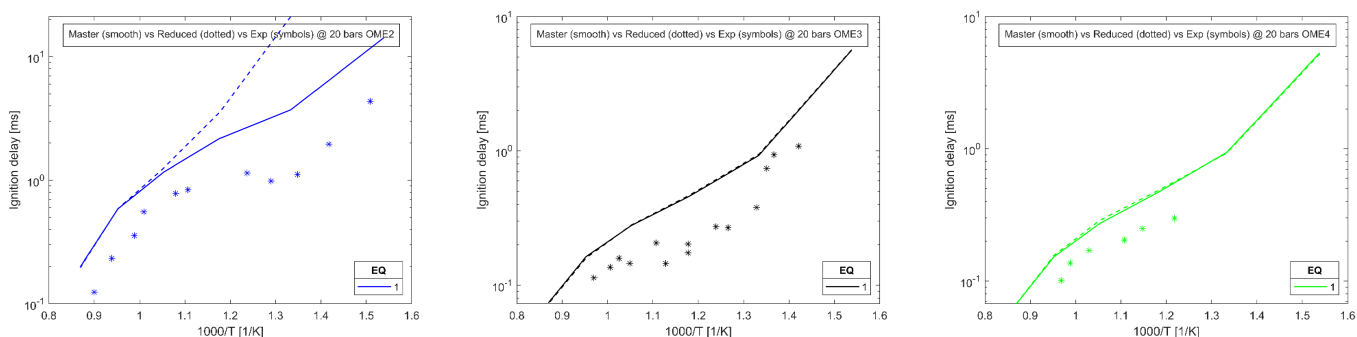
Figure 20: Ignition delay comparison between master, reduced and experimental values for individual fuel components.

4.3.2 Laminar Flame Speed

Laminar flame speed validations have been critical to evaluate a reaction mechanism. Simulations regarding laminar flame speed were performed in a CHEMKIN flame speed calculator at different equivalence ratios and specific temperature. The experimental data set was taken from already published study related to OME$_3$ [22]. The Figure 21 below shows an agreement of both reduced and master mechanism with the experimental data set.
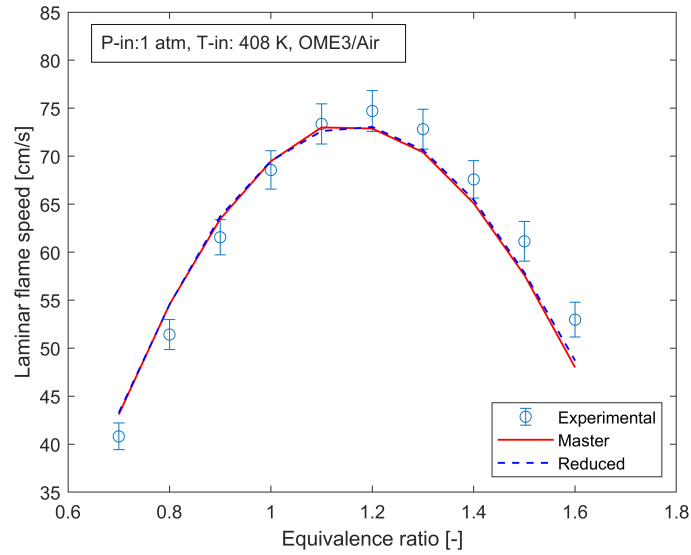
Figure 21: laminar flame speed comparison between master and reduced mechanism and experimental values.

4.3.3 3D CFD Simulation

The reduced mechanism of OME_3 was then implemented in a 3D CFD simulation to see its validity. The engine data used in this simulation was the one already configured so here no details have been added. The below Figure 22 shows the heat release rate obtained by performing 3D CFD simulations in CONVERGE CFD. It can be seen that the HRR is well in agreement with the master mechanism data. Besides, it is possible to see that the model is able to predict certain characteristic behaviour of the experiments even with a complex injection strategy (2 pilot - 1 main - 1 post injection) like the one used here.
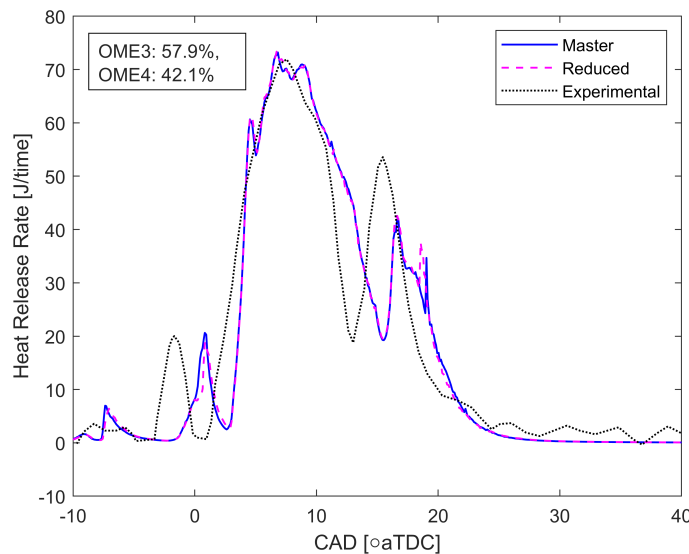
Figure 22: Heat release rate comparison between master and reduced mechanism and experimental values.

4.4 Future Work

The future work that could be done related to the above developed study has many possibilities. Some of the steps that could be taken are described as follows:

- The input test matrix related to the reduction of the mechanism could be extended to include for example, various number of fuel compositions, a wide range of pressures or equivalence ratios, ultimately to widen the possibility of utilization of reduced mechanism and get realistic results as much closer as possible to experimental fuels being used.

- The reduced OME_x mechanism developed could be merged with other PRF/PAH mechanisms to be utilized in case of fuels having blends with OME_x.

- Further, this reduction technique could be extended to other fuels and their combinations like OME_1 and hydrogenated vegetable oil (HVO), ultimately to develop compact yet robust mechanisms for these synthetic fuels that are much less expensive in terms of computational cost.

5 Conclusions

The aim of this work has been to deepen into understanding how the properties and the stoichiometry of OME_x affect the combustion process and pollutant formation of OME_x-fossil fuel blends in a CI engine when the composition is varied within a wide range (from 10 to 50% of OME_x content in the mixture). For this purpose, CFD simulations of a medium duty optical engine has been performed using n-heptane (Diesel) and OME_3 (OME_x) as surrogate fuels: Besides, experimental data obtained at the same optical engine has been used to corroborate the numerical results.

First, different reaction mechanism from literature were evaluated for these mixtures. The results showed that the most compact reaction mechanism provided by Lin 2019 [33] is able to reproduce a global combustion behaviour similar to the one observed with the experimental data. However, the other three mechanisms evaluated He 2017 [32], Ren 2019 [24], Lin 2021 [26] were providing larger ignition delays, which strongly affected the rest of the combustion process. Using the selected reaction mechanism, simulations of different blends of n-heptane and OME_3 were carried out. Further a reduced mechanism for OME_x was developed using different mechanism reduction techniques. The main conclusions obtained from the analysis of the data obtained are summarized here:

- The ignition delay of the blend decreases when increasing the OME_3 content and the trend tends asymptotically to a value similar to that of D50O50. This suggest that above 20% OME_3, the ignition delay of these blends is mostly controlled by the most reactive component.

- The HRR at the premixed combustion phase increased when decreasing the OME_3 fraction, which can be related with the lower LHV of this fuel but also with the different ID of the blends. On the other hand, the HRR levels reached during the diffusion phase are more similar despite the difference in terms of LHV. In addition, it has been also observed at the late stages of combustion that an increase of OME_3 content also increases the combustion speed up to 5% for D50O50 when compared to D90O10.

- The different stoichiometry of OME_3 leads to a decrease of the Φ field. In this sense, D50O50 provides a different behaviour than the other blends. The fact that it reaches lower Φ values

(closer to 1) is promoting oxidation reaction which result in a faster combustion completion and sooner OH disappearance.

- The higher Φ values reached when reducing the OME_3 content has been related with the higher net soot formation. On one hand, the soot formation increases as the amount of mixture under $\Phi > 2$ increases. On the other hand, the percentage of soot oxidation decreases too. This leads to a higher amount of soot in the cylinder, which lasts longer before being oxidized.

- The reduced mechanism developed for OME_x was validated effectively in terms of ignition delays, flame speeds and also worked effectively in terms of 3D CFD simulations making it a computationally less costly and effective replacement of original master mechanism.

Futhermore, the numerical simulation highlights the benefits of using OME_3 when partially replacing fossil Diesel in CI engines. The lower LHV of the fuel is a constraint but the faster oxidation process reported here would allow to increase injection duration to compensate for that. With low OME_3 percentages (below 20%) the soot decrease is not remarkable. However, for D70O30 and D50O50 more important differences were observed. This is interesting to reduce the soot-NO_x trade-off in this type of engines. However, a deeper study would be recommended under different operating conditions (e.g., with EGR) to confirm this. Finally, it is worth mentioning that the results obtained with numerical simulations have been corroborated with experimental data obtained in the same optical engine.

At last, it is noteworthy to mention that work related to section I and II is a part of a journal paper found at (https://doi.org/10.1016/j.fuel.2022.124768) and section III related to mechanism reduction will be basis of other publication in future.

References

[1] A. García, J. Monsalve-Serrano, R. L. Sari, and S. Martinez-Boggio, "Influence of environmental conditions in the battery thermal runaway process of different chemistries: Thermodynamic and optical assessment," *International Journal of Heat and Mass Transfer*, vol. 184, p. 122381, 2022.

[2] A. García, J. Monsalve-Serrano, R. L. Sari, and S. Tripathi, "Pathways to achieve future co2 emission reduction targets for bus transit networks," *Energy*, p. 123177, 2022.

[3] J. V. Pastor, A. García, C. Micó, F. Lewiski, A. Vassallo, and F. C. Pesce, "Effect of a novel piston geometry on the combustion process of a light-duty compression ignition engine: An optical analysis," *Energy*, vol. 221, p. 119764, 2021.

[4] W. Deng, Q. Hu, T. Liu, X. Wang, Y. Zhang, W. Song, Y. Sun, X. Bi, J. Yu, W. Yang, *et al.*, "Primary particulate emissions and secondary organic aerosol (soa) formation from idling diesel vehicle exhaust in china," *Science of the Total Environment*, vol. 593, pp. 462–469, 2017.

[5] A. García, J. Monsalve-Serrano, S. Martínez-Boggio, and K. Wittek, "Potential of hybrid powertrains in a variable compression ratio downsized turbocharged vva spark ignition engine," *Energy*, vol. 195, p. 117039, 2020.

[6] J. V. Pastor, A. García, C. Micó, and F. Lewiski, "Simultaneous high-speed spectroscopy and 2-color pyrometry analysis in an optical compression ignition engine fueled with omex-diesel blends," *Combustion and Flame*, vol. 230, p. 111437, 2021.

[7] H. L. Chum and R. P. Overend, "Biomass and renewable fuels," *Fuel processing technology*, vol. 71, no. 1-3, pp. 187–195, 2001.

[8] A. García, J. Monsalve-Serrano, D. Villalta, and M. Guzmán-Mendoza, "Parametric assessment of the effect of oxygenated low carbon fuels in a light-duty compression ignition engine," *Fuel Processing Technology*, vol. 229, p. 107199, 2022.

[9] L. Grégoire, F.-L. Vincent, E. Damien, J. M. Christoph, and S. L. Klaus, "Electricity storage with liquid fuels in a zone powered by 100% variable renewables," in *2015 12th International Conference on the European Energy Market (EEM)*, pp. 1–5, IEEE, 2015.

[10] Y. He, L. Zhu, J. Fan, L. Li, and G. Liu, "Life cycle assessment of co2 emission reduction potential of carbon capture and utilization for liquid fuel and power cogeneration," *Fuel Processing Technology*, vol. 221, p. 106924, 2021.

[11] J. V. Pastor, J. M. García-Oliver, C. Micó, A. A. García-Carrero, and A. Gómez, "Experimental study of the effect of hydrotreated vegetable oil and oxymethylene ethers on main spray and combustion characteristics under engine combustion network spray a conditions," *Applied Sciences*, vol. 10, no. 16, p. 5460, 2020.

[12] J. V. Pastor, J. M. Garcia-Oliver, C. Micó, and F. J. Tejada, "Combustion behaviour of blends of synthetic fuels in an optical single cylinder engine," tech. rep., SAE Technical Paper, 2021.

[13] Y. Zheng, Q. Tang, T. Wang, Y. Liao, and J. Wang, "Synthesis of a green fuel additive over cation resins," *Chemical Engineering & Technology*, vol. 36, no. 11, pp. 1951–1956, 2013.

[14] B. Lumpp, D. Rothe, C. Pastötter, R. Lämmermann, and E. Jacob, "Oxymethylene ethers as diesel fuel additives of the future," *MTZ worldwide eMagazine*, vol. 72, no. 3, pp. 34–38, 2011.

[15] A. Omari, B. Heuser, and S. Pischinger, "Potential of oxymethylenether-diesel blends for ultra-low emission engines," *Fuel*, vol. 209, pp. 232–237, 2017.

[16] A. García, J. Monsalve-Serrano, D. Villalta, R. L. Sari, V. G. Zavaleta, and P. Gaillard, "Potential of e-fischer tropsch diesel and oxymethyl-ether (omex) as fuels for the dual-mode dual-fuel concept," *Applied Energy*, vol. 253, p. 113622, 2019.

[17] J. V. Pastor, A. García, C. Micó, and F. Lewiski, "An optical investigation of fischer-tropsch diesel and oxymethylene dimethyl ether impact on combustion process for ci engines," *Applied Energy*, vol. 260, p. 114238, 2020.

[18] A. Damyanov, P. Hofmann, B. Geringer, N. Schwaiger, T. Pichler, and M. Siebenhofer, "Biogenous ethers: Production and operation in a diesel engine," *Automotive and Engine Technology*, vol. 3, no. 1, pp. 69–82, 2018.

[19] J. Benajes, A. García, J. Monsalve-Serrano, and S. Martínez-Boggio, "Potential of using omex as substitute of diesel in the dual-fuel combustion mode to reduce the global co2 emissions," *Transportation Engineering*, vol. 1, p. 100001, 2020.

[20] C. Hank, L. Lazar, F. Mantei, M. Ouda, R. J. White, T. Smolinka, A. Schaadt, C. Hebling, and H.-M. Henning, "Comparative well-to-wheel life cycle assessment of ome 3–5 synfuel production via the power-to-liquid pathway," *Sustainable Energy & Fuels*, vol. 3, no. 11, pp. 3219–3233, 2019.

[21] R. Novella, A. García, J. M. Pastor, and V. Domenech, "The role of detailed chemical kinetics on cfd diesel spray ignition and combustion modelling," *Mathematical and Computer Modelling*, vol. 54, no. 7-8, pp. 1706–1719, 2011.

[22] W. Sun, G. Wang, S. Li, R. Zhang, B. Yang, J. Yang, Y. Li, C. K. Westbrook, and C. K. Law, "Speciation and the laminar burning velocities of poly (oxymethylene) dimethyl ether 3 (pomdme3) flames: An experimental and modeling study," *Proceedings of the Combustion Institute*, vol. 36, no. 1, pp. 1269–1278, 2017.

[23] T. He, Z. Wang, X. You, H. Liu, Y. Wang, X. Li, and X. He, "A chemical kinetic mechanism for the low-and intermediate-temperature combustion of polyoxymethylene dimethyl ether 3 (pode3)," *Fuel*, vol. 212, pp. 223–235, 2018.

[24] S. Ren, Z. Wang, B. Li, H. Liu, and J. Wang, "Development of a reduced polyoxymethylene dimethyl ethers (poden) mechanism for engine applications," *Fuel*, vol. 238, pp. 208–224, 2019.

[25] D. Lv, Y. Chen, Y. Chen, X. Guo, H. Chen, and H. Huang, "Development of a reduced diesel/poden mechanism for diesel engine application," *Energy Conversion and Management*, vol. 199, p. 112070, 2019.

[26] Q. Lin, K. L. Tay, F. Zhao, and W. Yang, "Enabling robust simulation of polyoxymethylene dimethyl ether 3 (pode3) combustion in engines," *International Journal of Engine Research*, p. 14680874211018363, 2021.

[27] K. Richards, P. Senecal, and E. Pomraning, "Converge 3.0; convergent science: Madison, wi, usa, 2021."

[28] J. V. Pastor, J. M. Garcia-Oliver, C. Micó, and F. J. Tejada, "Combustion behaviour of blends of synthetic fuels in an optical single cylinder engine," SAE International, 9 2021.

[29] F. Payri, P. Olmeda, J. Martín, and A. García, "A complete 0d thermodynamic predictive model for direct injection diesel engines," *Applied Energy*, vol. 88, no. 12, pp. 4632–4641, 2011.

[30] W. J. Pitz and C. J. Mueller, "Recent progress in the development of diesel surrogate fuels," *Progress in Energy and Combustion Science*, vol. 37, no. 3, pp. 330–350, 2011.

[31] A. Diez, R. J. Crookes, and T. Løvås, "Experimental studies of autoignition and soot formation of diesel surrogate fuels," *Proceedings of the Institution of Mechanical Engineers, Part D: Journal of Automobile Engineering*, vol. 227, no. 5, pp. 656–664, 2013.

[32] T. He, H.-y. Liu, Y. Wang, B. Wang, H. Liu, and Z. Wang, "Development of surrogate model for oxygenated wide-distillation fuel with polyoxymethylene dimethyl ether," *SAE International Journal of Fuels and Lubricants*, vol. 10, no. 3, pp. 803–814, 2017.

[33] Q. Lin, K. L. Tay, D. Zhou, and W. Yang, "Development of a compact and robust poly-oxymethylene dimethyl ether 3 reaction mechanism for internal combustion engines," *Energy Conversion and Management*, vol. 185, pp. 35–43, 2019.

[34] D. L. Siebers, "Scaling liquid-phase fuel penetration in diesel sprays based on mixing-limited vaporization," *SAE transactions*, pp. 703–728, 1999.

[35] P. O'rourke and A. Amsden, "A particle numerical model for wall film dynamics in port-injected engines," *SAE transactions*, pp. 2000–2013, 1996.

[36] A. A. Amsden and M. Findley, "Kiva-3v: A block-structured kiva program for engines with vertical or canted valves," tech. rep., Lawrence Livermore National Lab.(LLNL), Livermore, CA (United States), 1997.

[37] R. I. Issa, "Solution of the implicitly discretised fluid flow equations by operator-splitting," *Journal of computational physics*, vol. 62, no. 1, pp. 40–65, 1986.

[38] P. Senecal, E. Pomraning, K. Richards, T. Briggs, C. Choi, R. McDavid, and M. Patterson, "Multi-dimensional modeling of direct-injection diesel spray liquid length and flame lift-off length using cfd and parallel detailed chemistry," *SAE transactions*, pp. 1331–1351, 2003.

[39] S. L. Hovden, "Undersøkelse av reaksjonsmekanismer for omebrennstoff for bruk til imple-mentering i 3d-cfd simulering av forbrenning," Master's thesis, The University of Bergen, 2019.

[40] Z. Wang, L. Li, J. Wang, and R. D. Reitz, "Effect of biodiesel saturation on soot formation in diesel engines," *Fuel*, vol. 175, pp. 240–248, 2016.

[41] T. Kitamura, T. Ito, J. Senda, and H. Fujimoto, "Mechanism of smokeless diesel combustion with oxygenated fuels based on the dependence of the equivalence ration and temperature on soot particle formation," *International Journal of Engine Research*, vol. 3, no. 4, pp. 223–248, 2002.

[42] L. Cai, S. Jacobs, R. Langer, F. vom Lehn, K. A. Heufer, and H. Pitsch, "Auto-ignition of oxymethylene ethers (omen, n= 2–4) as promising synthetic e-fuels from renewable electricity: shock tube experiments and automatic mechanism generation," *Fuel*, vol. 264, p. 116711, 2020.

[43] Z. Jing, C. Zhang, P. Cai, Y. Li, and J. Wang, "Construction of a reduced diesel/polyoxymethylene dimethyl ether 3 (pode3) reaction mechanism for combustion and emission analysis," *Energy & Fuels*, vol. 35, no. 5, pp. 4437–4446, 2021.